ACS APPLIED MATERIALS & INTERFACES

www.acsami.org

Research Article

Unraveling the Nanosheet Zeolite-Catalyzed Combustion of Aluminum Nanoparticles-Doped exo-Tetrahydrodicyclopentadiene (JP-10) Energetic Fuel

Dababrata Paul, Souvick Biswas, Hyeonji Yeom, Kyungsu Na,* Michelle L. Pantoya,* and Ralf I. Kaiser*

Cite This: *ACS Appl. Mater. Interfaces* 2024, 16, 53938−53949

Read Online

ACCESS | Metrics & More | Article Recommendations | Supporting Information

ABSTRACT: Nanosheet MFI zeolites (Zeolite Socony Mobil, five) have grown in popularity in cracking catalysis considering their tunability in porous topologies, acidic sites, and sheet thickness, thus allowing them to selectively adsorb molecules of specific sizes, shapes, and polarities, resulting in improved cracking performance for a specific fuel. Five different MFI zeolites in the form of a mesoporous nanosheet structure with a controlled concentration of acidic sites denoted as NSMFI(y), where y is Si/Al ratio, have been synthesized. The effects of the relative acidity content of these NSMFI(y) samples on the zeolite-catalyzed combustion of aluminum nanoparticles (AlNPs)-aided exo-tetrahydrodicyclopentadiene (JP-10) mixed energetic fuel droplets levitated in an oxygen−argon atmosphere were investigated using time-resolved imaging (optical and thermal infrared) and spectroscopic techniques (UV−vis and FTIR). The addition of 1.0 wt % of NSMFI(y) zeolites to AlNPs-JP-10 fluid fuel results in critically reduced ignition delays (9 ± 2 ms), elevated ignition temperatures (2800 ± 170 K), and prolonged burning times (60 ± 10 ms) with an enhanced combustion efficiency. The NSMFI(y) zeolites, which possess high acidity and significant mesoporosity, play a crucial role in improving the combustion efficiency by effectively catalyzing the chemical activation of JP-10 and prolonging the burning of the igniting droplet. The NSMFI (60) variant with the highest acidic site content achieved a maximum combustion efficiency of 80 ± 6%. A comprehensive catalytic combustion mechanism has been elucidated based on the detected reactive intermediates such as hydroxyl radical (OH) and aluminum monoxide (AlO). These findings will help to critically advance the development of next-generation, sustainable, and innovative mixed nanofluid fuels.

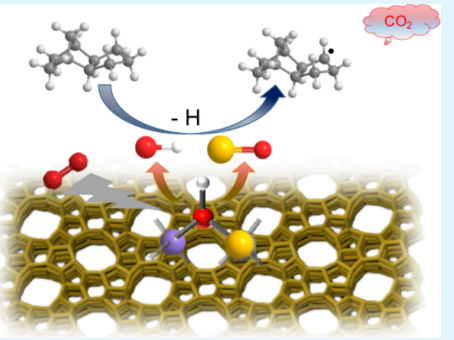

KEYWORDS: *nanofluid fuel, nanosheet MFI zeolite, fuel additives, exo-tetrahydrodicyclopentadiene (JP-10), droplet combustion chemistry, reaction intermediates, ultrasonic levitation*

1. INTRODUCTION

Nanofuels, hydrocarbon fuels mixed with metal-based nanoadditives, exhibit exceptional performance compared to pure hydrocarbon fuels and have garnered significant interest in the advancement of volume-limited air-breathing propulsion systems.[1−8] JP-10 (exo-tetrahydrodicyclopentadiene, $C_{10}H_{16}$) has emerged as one of the most promising synthetic single component hydrocarbon jet fuel[9−13] due to its high energy density (39.6 kJ cm^{-3}) and desirable thermophysical properties, such as low freezing point (−79 °C), and low flash point (54 °C).[14,15] Aluminum nanoparticles (AlNPs, energy density: 84 kJ cm^{-3}) have been proven as an efficient catalyst for decreasing ignition delays, boosting fuel flame temperatures, and facilitating thermal degradation of hydrocarbon fuels, such as JP-10.[1−3,15−17] However, the usage of AlNPs in JP-10 fluid fuel may causes NPs to agglomerate, resulting in lower dispersion stability and less sustainable combustion of AlNPs−JP-10 mixed fuel.[16,18,19] Zeolites, a specific catalyst made up of aluminosilicates possessing a higher surface area, better hydrothermal stability, and superior shape selectivity have been contemplated as ideal catalysts for hydrocarbon cracking.[18,20−27]

The catalytic activity of zeolites is quite diverse, affecting both chemical and size-dependent mechanisms. The advancement of synthetic approaches and characterization techniques has enabled the fabrication of desirable zeolite materials with a variety of physiochemical properties, such as framework compositions, acidic site inclusion, and structural morphologies. As a result, these materials have become popular as industrial catalysts in cracking, as absorbents and ion exchangers, in isomerization processes, and hydrocarbon synthesis.[18,20,23,26,28] Chemically, acidic sites are characterized

Received: July 19, 2024
Revised: September 18, 2024
Accepted: September 18, 2024
Published: September 30, 2024

as the presence of a hydroxyl group bridging Al and Si (Bronsted acid) and extra-framework aluminum (Lewis acid), which is usually determined via silicon dioxide (SiO_2) to aluminum oxide (Al_2O_3) ratios or simply via Si/Al ratios. The total acidic sites along with the types of cations (H^+, Na^+, K^+, Li^+) in the structural framework are crucial factors in the process of catalytic cracking of hydrocarbon fuels. On the other hand, distinct zeolites have unique porous architectures that selectively adsorb molecules of specific sizes, shapes, and polarities, resulting in improved catalytic cracking performance for the reactions that are difficult or technically inaccessible for conventional catalysts.[25] Considering the pore size of zeolites, microporous zeolites (ZSM-5, possessing pore diameter: 0.51−0.56 nm), however, have poor diffusion efficiency for catalytic cracking or combustion of large molecules, such as JP-10 (size: 0.67 nm × 0.38 nm).[18] The fabrication of the nanosheet zeolite with pore diameters extended to meso or macro pore sizes and diffusion lengths (determined by the thickness on nanosheet) limiting to nanometers can considerably improve diffusion efficiency and access to extended acidic sites to the reactants, resulting in effective catalytic performance.[18,29−33] For example, compared to standard HZSM-5 having MFI structure, nanosheet HZSM-5 provided 30% greater conversions for catalytic cracking of *n*-heptane.[34,35] In addition, a substantial quantity of mesopore volume between the sheets was maintained in the unilamellar nanosheet MFI zeolite. Alternatively, acidic sites' accessibility can also be improved by incorporating an enhanced fraction of Al_2O_3 materials in their structure.[36]

Here, considering these effects, MFI zeolites in the form of a mesoporous nanosheet structure with controlled concentration of acidic sites denoted as NSMFI(y), where y is the Si/Al ratio varying with 60, 80, 100, 125, and 150 were fabricated and tested to explore how NSMFI(y) zeolites with variable acidic site content influence the combustion efficiency against AlNPs-JP-10 mixed energetic fuels. In order to assess the combustion efficiency of NSMFI(y) zeolite materials to AlNPs-JP-10 energetic fuels, we explored the combustion of single levitating droplets, mimicking those formed in liquid fuel injection systems initiated through heating with a carbon dioxide laser; we subsequently recorded the combustion behavior by synchronized and temporally resolved imaging (thermal and optical) and spectroscopic techniques (UV−vis emission and Fourier transform infrared absorption spectroscopy). In these processes, the NSMFI(y) zeolite seeded AlNPs-JP-10 droplet expands initially upon heating due to the diffusional trapping of highly volatile species generated in the system, resulting in catalytic micro explosions and sustainable combustion with extended burning time. NSMFI(y) zeolites with extended mesoporosities with diameters of 7.5 ± 0.5 nm furnish JP-10 with individual compartments, leading to microexplosion. A time-resolved systematic study of the combustion of AlNPs-JP-10 fluid fuels doped with 1% by weight of NSMFI(y) zeolite material droplets revealed superior combustion efficiency with enhanced burning periods, and the underlying reaction mechanism has been unravelled based on the detection of reactive intermediates. This foundational study on the combustion of acoustically levitated NSMFI(y) zeolite-doped AlNPs-JP-10 droplets could aid in the development of next-generation sustainable revolutionary multicomponent nanofluid fuels.

2. MATERIAL AND METHODS

2.1. Materials. JP-10 ($C_{10}H_{16}$, purity ≥ 98%) was purchased from BOC science and used without further purification. AlNPs (diameter: 80 nm, purity = 99.99%) and NSMFI(y) zeolite materials were prepared at Texas Tech University, U.S.A. and Chonnam National University, S. Korea, respectively and reported earlier.[37,38] In brief, the NSMFI(y) zeolite materials were synthesized using the quaternary ammonium surfactant (denoted as $C_{22-6-6}Br_2$) as the hierarchically unilamellar structure directing agent.[29,38] The detailed procedure of $C_{22-6-6}Br_2$ synthesis is available in the Supporting Information. In a typical synthesis of NSMFI(y) zeolites, water glass (29 wt % aqueous solution, Si/Na = 1.57, DAEJUNG), sodium aluminate (41 wt % Na_2O, 53 wt % Al_2O_3, Na/Al = 1.27, Sigma-Aldrich), H_2SO_4 (98%, Daejung), $C_{22-6-6}Br_2$, and distilled water were used to obtain a gel composition of xAl_2O_3:(31.8 + 0.7x)-Na_2O:100SiO_2:7.5$C_{22-6-6}Br_2$:24H_2SO_4:4000H_2O, wherein x was assigned value as 0.833, 0.625, 0.5, 0.4, and 0.333 for the desired Si/Al ratio. At first, the water glass solution was added to the surfactant solution all at once while vigorously stirring using a magnetic stirrer at room temperature. To this solution was added an aqueous solution of sodium aluminate dropwise under vigorous stirring. Thereafter, an aqueous solution of H_2SO_4 was rapidly added to this solution. The resultant mixture was immediately shaken by hand or with a mechanical stirrer for 5 min to obtain a homogeneous gel. After further stirring for 6 h with a magnetic stirrer in an oven at 60 °C, the gel mixture was transferred to a Teflon-lined stainless steel autoclave and heated at 150 °C for 4−5 days with a rotation of 60 rpm. Under hydrothermal conditions at a high temperature, this extended synthesis period is necessary for the development of a well-ordered crystalline zeolite structure. The products were filtered and washed with distilled water and then dried in an oven at 130 °C. All of the zeolites were calcined at 550 °C for 4 h under air flow. The resultant nanosheet zeolites are denoted as NSMFI(y) in which y refers to the Si/Al ratios of 60, 80, 100, 125, and 150.

2.2. Sample Preparation. Five samples of AlNPs-JP-10 doped with different NSMFI(y) zeolites were prepared by mixing as low as 1 wt % of each of the AlNPs powder and zeolite of NSMFI(60), NSMFI(80), NSMFI(100), NSMFI(125), and NSMFI(150) with JP-10. All samples were sonicated for 30 min to ensure that the AlNPs and zeolite materials were evenly dispersed and no suspensions were seen during the experiment. JP-10 containing 2 wt % AlNPs was also prepared as a reference system for fair comparison with 1 wt % each of AlNPs and zeolites in JP-10. It should be noted that 2 wt % AlNPs is the threshold concentration for JP-10 combustion. Prior to the combustion study, Raman analysis was also conducted on each sample to ascertain whether the combination of AlNPs and NSMFI(y) zeolite materials with JP-10 resulted in the formation of new species or any other intermolecular interactions that altered the fundamental properties of each component in the multicomponent systems. The characteristics features of NSMFI(y) zeolites and NSMFI(y) zeolites doping into AlNPs-JP-10 samples are presented in Figures S4 and S5, and listed in Tables S2 and S3, respectively. It should be noted that the addition of zeolites to the AlNPs-JP-10 fluid does not disrupt individual frequencies.

2.3. Methods. The combustion of singly levitated NSMFI(y) zeolites doped AlNPs-JP-10 energetic fuel droplets was investigated using an ultrasonic levitator in association with a time-resolved UV−vis, IR, Raman, optical, and thermal imaging laboratory simulation setup (Scheme 1 and Figure S1). The detail of levitation setup has been described previously.[39−44] In brief, the levitator consists of a piezoelectric transducer with a 58 kHz oscillation frequency and a concave-shaped reflector. The reflection of ultrasonic sound waves between the transducer and the reflector generates a standing wave with five pressure nodes; the acoustic radiation pressure counterbalances the gravitational pull, lifting the droplet slightly below one of the standing wave's pressure nodes at position three. This ultrasonic levitator is mounted in a pressure-compatible stainless-steel process chamber. Nanofluid fuel samples were injected using a homemade droplet deposition technique, resulting in the creation of oblate

https://doi.org/10.1021/acsami.4c12078
ACS Appl. Mater. Interfaces 2024, 16, 53938−53949

Scheme 1. (A) Top View of the Levitator System Displaying the Ultrasonic Levitator, Process Chamber, Carbon Dioxide Laser, Raman Spectrometer, FTIR Spectrometer, Fiber Optic UV-Vis Spectrometer, Infrared Camera, and Optical Camera; (B) Pulse Sequence for the Experimental Setup at Time to Collect Reference Spectra and Reference Images

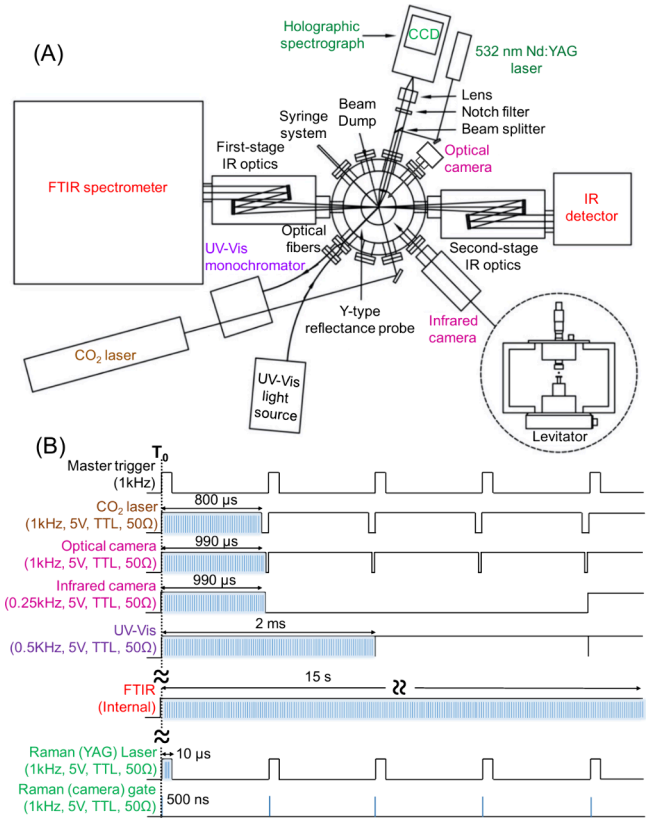

spheroidal droplets (typical volume of about 10 ± 0.5 μL) within the pressure node. The droplets were levitated in a controlled environment of 20% oxygen (O_2, 99.99% Airgas) and 80% argon (Ar, 99.99% Airgas) at a total pressure of 800 ± 20 Torr to surpass the rational ignition conditions.

The levitated droplets were heated by a CO_2 laser beam with an output of 32 ± 2 W at 10.6 μm, exceeding the ignition threshold of the current droplets. Upon ignition, the combustion features were characterized using time-resolved ultraviolet−visible (UV−vis) and Fourier-transform infrared (FTIR) spectroscopies along with an IR thermal-imaging and a high-speed optical camera. UV−vis spectra were captured 1 cm away from the droplet combustion by a fiber optic probe of a UV−vis spectrometer (StellarNet SILVER-Nova) covering the wavelength range 200−1100 nm with a spectral resolution of 2 nm and a temporal resolution of 1 ms. The FTIR spectra were collected using a Nicolet 6700 FTIR spectrometer over the wavelength range of 500−5000 cm^{-1} immediately following each droplet combustion to avoid any deactivation of the gaseous species formed.

A Phantom Miro 3a10 camera equipped with a Navitar Zoom 6000 modular lens system recorded the videos of ignition events at a frame rate of 1000 frames per second (fps). Additionally, an FLIR A6703sc infrared camera recorded the thermal-imaging videos of the ignition process. The droplets were also characterized by our home-built Raman spectrometer using a Q-switched Nd:YAG laser (CrystaLaser, model QL532-1W0), where the scattered light from the sample was collected through a convex lens followed by passing through an ultrasteep long-pass edge filter (Semrock, model LP03-532RE-25) to eliminate the elastically scattered 532 nm laser light and ultimately detected by HoloSpec f/1.8 holographic imaging spectrograph (Kaiser Optical Systems, model 2004500-501 and Holoplex HPG-532) equipped with a PI-Max 2 ICCD camera (Princeton Instruments) through a slit (width = 100 μm). The optical specifications and calibration procedure for the Raman spectrometer can be found in the Supporting Information. All of the measurements were performed at least three times to ensure the maximum reproducibility of the combustion process.

3. RESULTS AND ANALYSIS

3.1. NSMFI(*y*) Zeolites Characterization. The unilamellar structural motif with mesoporosity of five NSMFI(y) zeolites, NSMFI(60), NSMFI(80), NSMFI(100), NSMFI(125), and NSMFI(150) with regulated Si/Al ratios (Figure 1A) was validated by scanning electron microscopy (SEM), transmission electron microscopy (TEM), Raman, X-ray diffraction (XRD), and N_2 sorption analysis. Figure 2A shows high-resolution SEM images of the materials, revealing their general forms and surface roughness. The mesopores of the crystal unit can be easily identified between the randomly distributed nanosheets. The individual nanosheets get shaper when the Si/Al ratio increases. The TEM images (Figure 2B) depict highly crystalline structures in the samples. Furthermore, self-pillar organization of ultrathin nanosheets is recognized confirming the formation of a unilamellar-like structure.[36] The thickness of the nanosheets in NSMFI(60) is found to be 2.21 nm, while it increases to 2.69 nm for NSMFI(150) (Figure 1C,D). Increased Si/Al ratios can result in thicker nanosheets due to fewer Al-induced distortions and reduced hydrogen bonding, which promotes crystal growth.[45,46] This observation confirms the variation in the Al content, which decreased from 0.833 to 0.333, in the zeolite samples.

Raman spectra reveal the key bonding motif of Si−O−Si and Si−O−Al in the crystal structure (Figure S4). The characteristics Raman peaks and bands corresponding to Si−O−Si and Si−O−Al modes are invariantly observed at positions with known bonds and functional group assignments, confirming the formation of MFI zeolites (Table S2).[47] The unilamellar structural motif was also further confirmed by XRD measurements (Figure 1E). Every synthetic zeolite material possesses typical crystalline XRD reflections that are very distinctive and follow the MFI structure (JCPDS no. 00−044−0002).

The mesoporosity of five rationally designed NSMFI(y) zeolite materials was characterized with a nitrogen (N_2) adsorption isotherms technique (Figure S2). The average pore diameter of each sample was extracted using the Barrett−Joyner−Halenda (BJH) algorithm (Figure 1F). Although the thickness of the nanosheets varies depending on the Si/Al ratios, there is no statistically significant alteration in the pore diameter, which remains constant at 7.5 ± 0.5 nm. Unlike the distribution of pore sizes, the zeolite samples exhibit a noticeable rise in acidic sites from 0.009 to 0.020 mmol g^{-1} (Figure S3 and Table S1).

3.2. Ignition Event. To visualize the ignition events, we recorded the synchronized and temporally resolved optical and infrared images on the combustion of AlNPs-JP-10 energetic fluid fuels containing NSMFI(y) zeolites. The time-resolved optical images of the entire event that were collected are shown in Figure S6, with a 5 ms interval between each image. Upon exposure to the carbon dioxide laser, the droplet expands significantly due to the diffusional entrapment of high velocity species NSMFI(y) and AlNPs, resulting in the formation of a gloomy cloud along with white sparkling at

https://doi.org/10.1021/acsami.4c12078
ACS Appl. Mater. Interfaces 2024, 16, 53938−53949

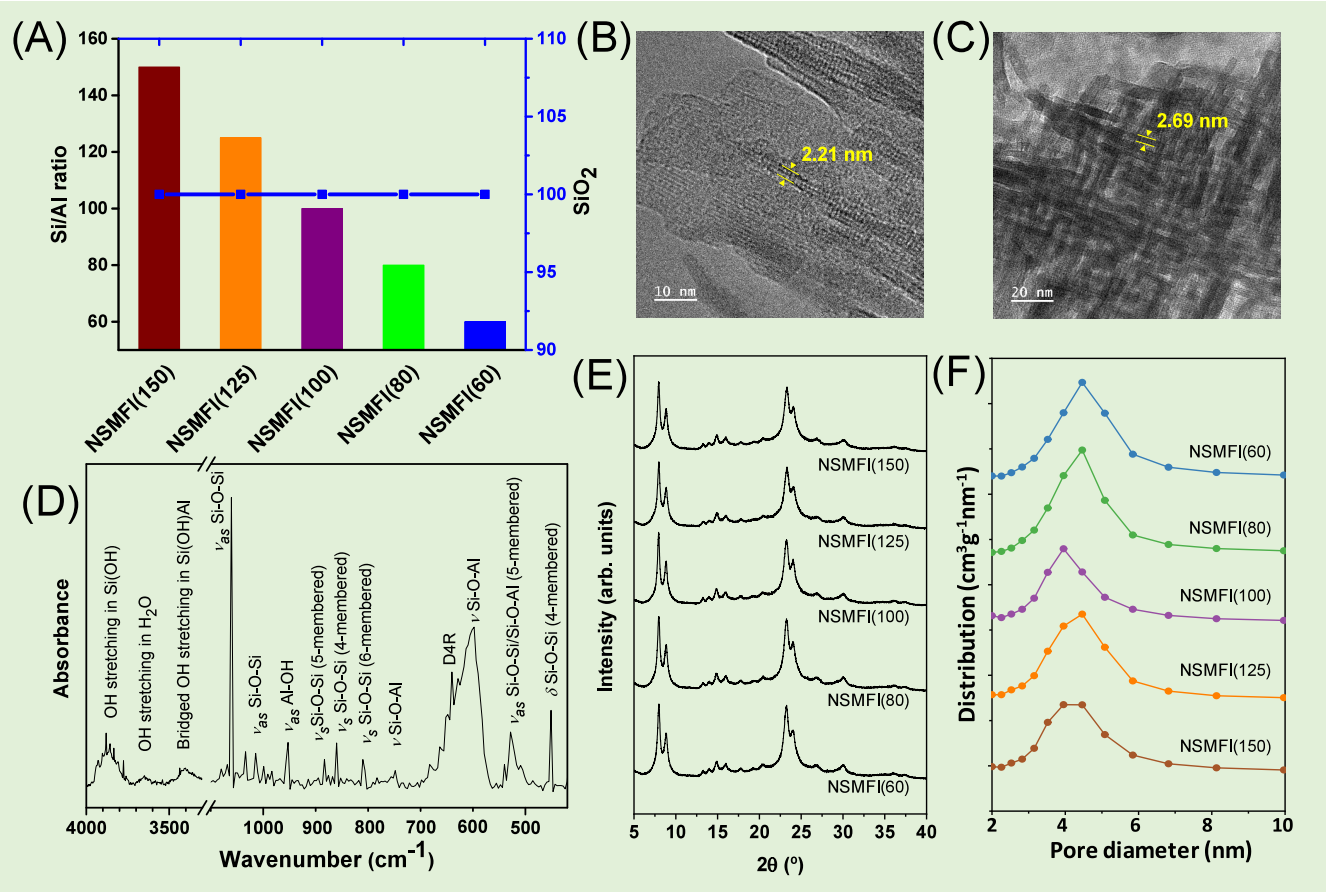

Figure 1. (A) Five nanosheet MFI zeolites: NSMFI(60), NSMFI(80), NSMFI(100), NSMFI(125), and NSMFI(150) with controlled Si/Al ratio. (B, C) HRTEM images of NSMFI(60) zeolite and NSMFI(150), respectively. The thickness of the nanosheets was also measured and depicted in the figures. Raman spectrum of NSMFI(60) is shown in (D). The Raman peaks and bands of the NSMFI(60) zeolite are assigned inside the figure. Wide-angle powder XRD patterns (E) and pore size distribution measured from N_2 adsorption isotherm (F) of five nanosheet MFI zeolites.

the center (lower panel of Figure 3A, and upper panel of Figure S6), followed by catalytic combustion (Figure S6, lower panel). As soon as the JP-10 autoignition temperature of 509 K is attained,[14] the flame quickly spreads over the nanofluid spray cloud displaying maximum brightness and combustion temperature (Figure 3A,C). The temperature profiles of each NSMFI(y)/AlNPs system show that the ignition delay, which is defined by the time difference between the initial laser shot and the commencement of the ignition point, along with the maximum temperature attained, varies with the overall textural properties of the NSMFI(y) zeolite materials (Figure 3E). The ignition delay time decreases from an average of 20 ± 3 ms for NSMFI(150)/AlNPs to an average of 9 ± 2 ms for NSMFI(60)/AlNPs, whereas the mean maximum temperature increases from 2580 ± 155 K to 2800 ± 170 K, respectively (Figure 3D,E). The system's high temperature is attained by the irradiation of a CO_2 laser beam on droplets of JP-10 containing nanomaterials (NSMFI(y) and AlNPs), which serve as heat transfer carriers, and postignition burning. The temperature fluctuations of radiated power are caused by the random burst out (a thermodynamically non-equilibrium process) of nanoparticles. To clarify the ignition delay and maximum flame temperature measured during the combustion of AlNPs-JP-10 energetic fuels with five NSMFI(y) zeolites, a reference system containing 2 wt % of AlNPs in JP-10 was used, as the nanofluid fuels being investigated consist of 1 wt % of both AlNPs and NSMFI(y) zeolites in JP-10. The ignition delay and achieving maximum temperature of 2 wt % of AlNPs nanoparticles in JP-10 is found to be 22 ± 3 ms and 1840 ± 120 K, respectively, under identical experimental conditions. However, under controlled circumstances, JP-10 containing 1 wt % of AlNPs or NSMFI(y) zeolites, individually did not combust.

To identify the key species as reaction intermediates, products, and individual atoms formed during the combustion, we recorded temporally resolved UV−vis emission spectra over 127 ms with data collection times of 1 ms per spectrum within the wavelength range of 200−1100 nm during the combustion. Figure 3B shows the observed spectra of NSMFI(60)/AlNPs, while Figure S7 shows the spectra of the other systems. The point of exposure was denoted as time zero, and the ignition stage began at 9 ms (Figure 3B, first red spectrum), which was consistently documented by both optical (upper panel, Figure 3A) and thermal imaging (Figure 3E, rising edge of the blue profile). After commencing ignition, flames remained active for a short length of time (15 ± 5 ms) before ceasing and reactivating, revealing two temporally separate stages. Two distinct stages were likewise seen in the combustion of the four remaining investigated nanofluid systems (Figure S7). Among the five NSMFI(y)/AlNPs zeolite systems studied herein, the intensity in the two stages varies significantly. Specifically, the average intensity is higher in the second stage compared to the first stage for the first three systems: NSMFI(60)/AlNPs, NSMFI(80)/AlNPs, and NSMFI(100)/AlNPs, whereas, it is

https://doi.org/10.1021/acsami.4c12078
ACS Appl. Mater. Interfaces 2024, 16, 53938−53949

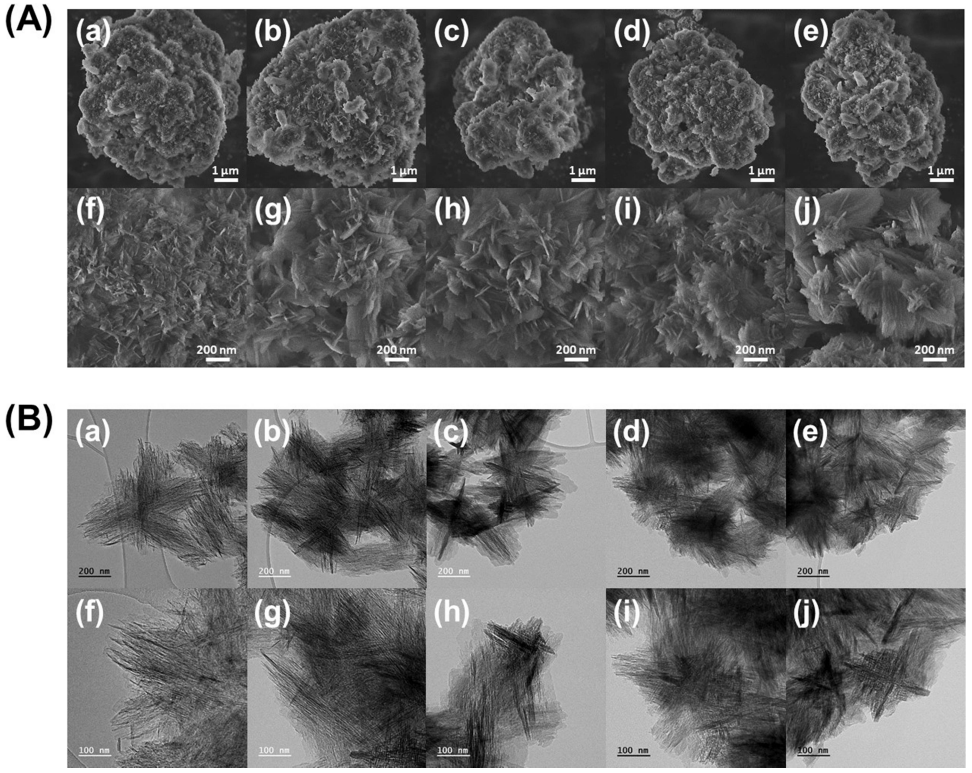

Figure 2. (A) SEM images of (a, f) NSMFI(60), (b, g) NSMFI(80), (c, h) NSMFI(100), (d, i) NSMFI(125), and (e, j) NSMFI(150) zeolites at low (top row) and high (bottom row) magnifications. (B) TEM images of (a, f) NSMFI(60), (b, g) NSMFI(80), (c, h) NSMFI(100), (d, i) NSMFI(125), and (e, j) NSMFI(150) zeolites at low (top row) and high (bottom row) magnifications.

less pronounced in the second stage for the remaining two systems: NSMFI(125)/AlNPs and NSMFI(150)/AlNPs. However, a single stage ignition event was detected for the reference system containing 2 wt % of AlNPs in the JP-10. A noteworthy observation in the UV−vis emission spectra of all systems containing NSMFI(y)/AlNPs zeolites is the longer burning time, measuring 60 ± 10 ms. Contrarily, the reference experiment with 2 wt % of AlNPs nanoparticles in JP-10 had a strict constraint on the combustion time, which was set at 20 ± 8 ms.

In order to enhance the visibility of the emission peaks, a blackbody background spectrum was subtracted in the region of special interest from 200 to 800 nm[7]. Figure 4A shows the deconvoluted spectrum of NSMFI(60)/AlNPs, and other deconvoluted spectra are shown in Supporting Information (Figure S8). The UV−vis peak/band center positions assigned to the individual species exhibited a higher level of concordance with the existing literature[48−50] and are listed in Table 1. The species hydroxyl (OH; $A^2\Sigma^+ \rightarrow X^2\Pi$), methylidyne (CH; $A^2\Delta \rightarrow X^2\Pi$), and water ($H_2O$), which are major intermediates or products of JP-10 combustion, along with atomic sodium (Na; $^2S_{1/2} - {}^2P_{1/2}$ and/or $^2S_{1/2} - {}^2P_{3/2}$), and diatomic aluminum monoxide (AlO; $A^2\Sigma^+ \rightarrow X^2\Sigma^+$) are identified. Traces of potassium as impurity are also detected in the emission spectra (K; $^2S_{1/2} - {}^2P_{3/2}$ and/or $^2S_{1/2} - {}^2P_{1/2}$). It should be noted that OH is either not detected or has a very weak signal within the noise level during the reference experiment of JP-10 combustion in the presence of 2 wt % of AlNPs. Instead, O_2 ($B^3\sum_u^- - X^3\sum_g^-$) is observed at a wavelength of 336 nm. It is apparent that the NSMFI(y) zeolites affect AlNPs-JP-10 combustion.

3.3. Detection of Gaseous Products and Combustion Efficiency. To identify the gaseous products generated during combustion, the FTIR spectra were collected for each droplet combustion, and combustion efficiency was calculated. The absorption characteristics of the five NSMFI(y) doped AlNPs-JP-10 zeolite systems, as well as the controlled AlNPs-JP-10 system, appeared to be comparable, with the same major features appearing in all systems (Figure 5). To improve visibility, the three sections (600−735, 2230−2420, and 2820−3000 cm^{-1}) were magnified, and all peaks or bands were labeled (a)−(k) within the figure and listed in Table S4. The observed peaks or bands of the vibrational modes of CO_2, H_2O, and unreacted JP-10 were consistent with the available literature.[51−53]

The combustion efficiencies were calculated based on the standard end products of the hydrocarbon (JP-10) via the following stoichiometric oxidation reaction: $C_{10}H_{16}(l) + 14O_2(g) \rightarrow 10CO_2(g) + 8H_2O(g)$, as JP-10 was the sole source of carbon. The two most intense bands, spanning from 2840 to 3000 cm^{-1} and from 2170 to 2460 cm^{-1}, were utilized to represent the stretching of C−H bonds in unreacted JP-10 and the antisymmetric stretching of CO_2, respectively, as the reactant and final product. The number densities or moles of CO_2 released during combustion were determined by using a calibration curve generated by measuring the intensities of certain bands as a function of different pressures of CO_2 in the process chamber under the same experimental conditions (Figure S10). The measured combustion efficiencies of five NSMFI(y) doped AlNPs-JP-10 zeolite systems and reference AlNPs-JP-10 system along with combustion and burn times are plotted in Figure 6. One important finding in this context is that the combustion efficiency is time-dependent and rises as

https://doi.org/10.1021/acsami.4c12078
ACS Appl. Mater. Interfaces 2024, 16, 53938−53949

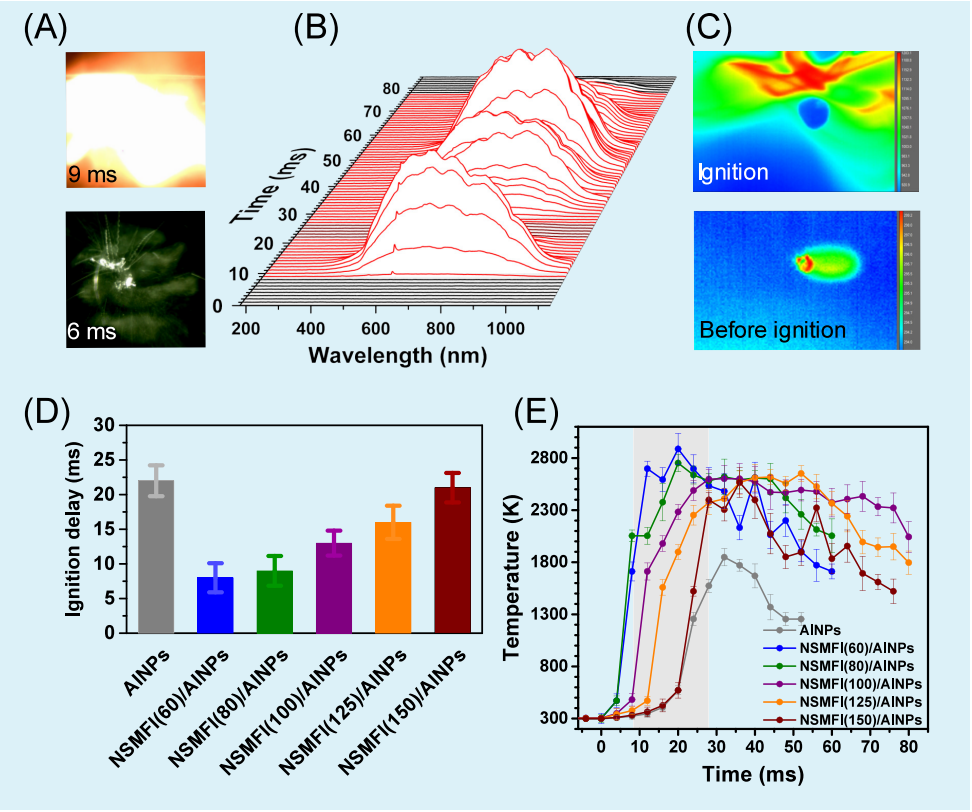

Figure 3. Synchronized and temporally resolved (A) optical images, (B) UV−vis emission spectra, and (C) thermal images during the ignition of the JP-10 droplet containing NSMFI(60)/AlNPs. The ignition delays and temperature profiles of AlNP-JP-10 nanofuel doped with five NSMFI(y) zeolite samples having controlled Si/Al ratios are shown in (D) and (E), respectively. For a reference JP-10 ignitions in the presence of 2% of AlNPs are also depicted in their respective ignition delay and temperature profile plots.

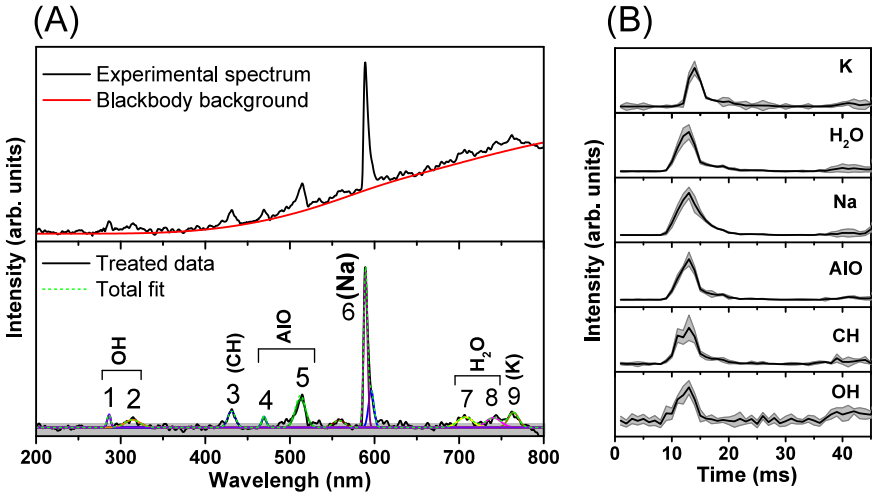

Figure 4. (A) UV−vis emission spectrum (upper panel) with blackbody radiation corrected and deconvoluted (bottom panel) for the identification of key species and their (B) temporal profiles during the ignition of JP-10 containing NSMFI(60)/AlNPs droplet. The black and red solid traces represent the experimental emission spectrum and blackbody radiation (A, upper panel). The black solid and green dot traces in the bottom panel reflect the treated data and each component's total fit, respectively. The vibrational mode assignments for the peaks or bands are listed in Table 1. All temporal profiles were obtained using the constrained linear least-squares method.[7]

the burning period lengthens. All systems that include zeolites have remarkably improved combustion efficiency, with percentages ranging from 41 to 80%. On the other hand, the combustion efficiency of the reference experiment, which contained 2 wt % of AlNPs nanoparticles in JP-10, was strictly limited to 28 ± 3%. Among the five zeolite systems, NSMFI(60)/AlNPs had the highest combustion efficiency at 80 ± 6%; the efficiency steadily declined to 41 ± 5% for NSMFI(150)/AlNPs as the Si/Al ratio increased.

https://doi.org/10.1021/acsami.4c12078
ACS Appl. Mater. Interfaces 2024, 16, 53938−53949

Table 1. Vibrational Mode Assignments for the Peaks and Bands in the Emission Spectrum of JP-10 Containing NSMFI(y)/AlNPs Droplets[a]

peak/band	peak/band center (nm)	molecule, atom, or radical	ref band (nm)	transition	vibrational quantum numbers (ν', ν'') or (ν_1', ν_2', ν_3') − (ν_1'', ν_2'', ν_3'')
1	286.8	OH	287.5−289.3	$A^2\sum^+ - X^2\Pi$	(2,1)
2	309.2	OH	309	$A^2\sum^+ - X^2\Pi$	(0,0)
2′	336	O_2	337	$B^3\sum_u^- - X^3\sum_g^-$	(0,14)
3	431.1	CH	431.4	$A^2\Delta - X^2\Pi$	(0,0)
4	468	AlO	467.2	$A^2\sum^+ - X^2\sum^+$	(2,1)
5	512.0	AlO	512.3	$A^2\sum^+ - X^2\sum^+$	(2,3)
6	589.1	Na	589.00	$^2S_{1/2} - {}^2P_{1/2}$	
			589.59	$^2S_{1/2} - {}^2P_{3/2}$	
7	707.8	H_2O	690−710	ro-vib. mode	(1,0,3)−(0,0,0)
8	743	H_2O	719−795	ro-vib. mode	(1,2,2)−(0,1,3)
9	766.6	K	767.50	$^2S_{1/2} - {}^2P_{3/2}$	
			769.90	$^2S_{1/2} - {}^2P_{1/2}$	

[a]2′ is applicable for reference system JP-10 with 2 wt % AlNPs only (Figure S8F).

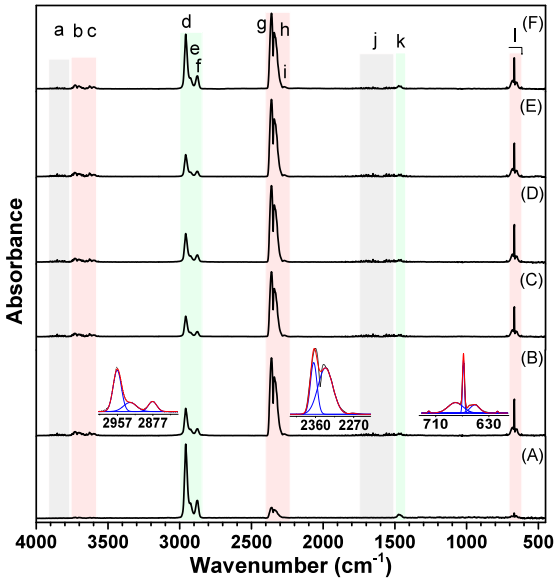

Figure 5. FTIR spectra after identification of gaseous products during ignition of JP-10 droplets doped with (A) AlNPs, (B) NSMFI(60)/AlNPs, (C) NSMFI(80)/AlNPs, (D) NSMFI(100)/AlNPs, (E) NSMFI(125)/AlNPs, and (F) NSMFI(150)/AlNPs. The bands of the products and unreacted JP-10 are assigned and listed in Table S4. The light red and gray shades represent the carbon dioxide (CO_2) and water (H_2O) reaction products, respectively, and the light green shade represents unreacted JP-10 vapor.

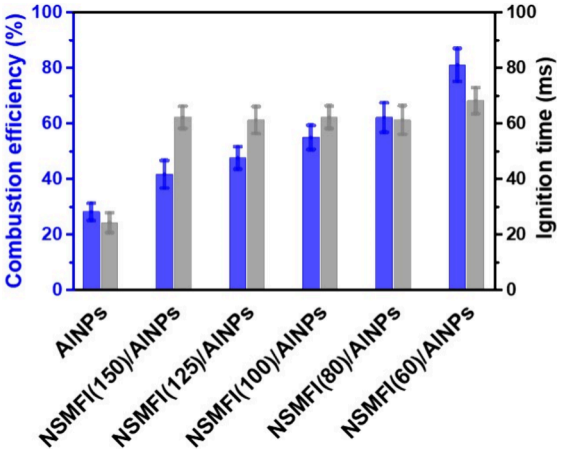

Figure 6. Plot showing the ignition time and combustion efficiency for JP-10 droplets containing AlNPs, NSMFI(60)/AlNPs, NSMFI(80)/AlNPs, NSMFI(100)/AlNPs, NSMFI(125)/AlNPs, and NSMFI(150)/AlNPs. Blue and gray columns stand for combustion efficiency and combustion time, respectively.

4. DISCUSSION

Before we engage in the discussion, we first compile all the key results of the experimental studies:

- The NSMFI(y) zeolites doped with AlNPs-JP-10 droplets exhibit a high propensity for ignition and have a significantly prolonged burning duration, leading to enhanced combustion efficiency. Therefore, the presence of NSMFI(y) zeolites is crucial for the ignition process and its underlying mechanism.
- The incorporation of NSMFI(y) zeolites to the AlNPs-JP-10 system resulted in a reduction of the ignition delay by 4 to 13 ms, and an increase in the maximum temperature by 750 to 950 K, depending on the Si/Al ratio of the zeolites, in turn depending on the concentration of acidic sites on external surfaces, implying improved ignition features of the AlNPs-JP-10 (Figure 3E).
- The UV−vis emission data revealed the presence of OH, CH, and H_2O, which are key intermediates and products of JP-10 combustion, along with dominance of atomic Na peak implies that NSMFI(y) zeolites also burn extensively upon ignition (Figures 4 and S8).
- Gas-phase AlO was also detected. The existence of reactive AlO in the flame, which can also enhance the combustion of JP-10, suggests that NSMFI(y) zeolites possess multiple mechanisms at action in the catalytic combustion of the AlNPs-JP-10 system.
- The time traces of the detected species confirm the simultaneous formation of Na with others OH, CH, AlO, and H_2O implying that the ignition was facilitated either by NSMFI(y) zeolites with AlNPs acting as heat transfer carriers, or by both zeolite and AlNPs.
- The FTIR data confirmed an accumulation of end products, namely, CO_2 and H_2O, in the combustion of JP-10. The dominant signal ratios of CO_2 (at 2170−2460 cm^{-1}) to unreacted JP-10 (2840−3000 cm^{-1}) of

https://doi.org/10.1021/acsami.4c12078
ACS Appl. Mater. Interfaces 2024, 16, 53938−53949

each zeolite system compared to reference system implies that NSMFI(y) zeolites significantly improve the catalytic combustion of AlNPs-JP-10 energetic fuel.

- The combustion efficiency increases from 41% to 80% when the acidity concentration of NSMFI(y) zeolites is raised from NSMFI(150) to NSMFI(60).

Zeolites represent excellent heterogeneous catalysts for hydrocarbon combustion due to their specific features, including high acidity and a distinctive structure. In order to ignite the primary fuel, JP-10 of AlNPs-JP-10 on NSMFI(y) zeolite catalysts, JP-10 molecules must either diffuse to acidic sites within the zeolite frameworks or come into close contact with zeolites during droplet expansion to ensure an effective catalyst−substrate interaction. The NSMFI(y) zeolites that we designed possess high acidity along with substantial porosity with a diameter of 7.5 ± 0.5 nm. Thus, NSMFI(y) zeolites provide a greater number of acid sites on their surface to the substrate than any other ZSM-5 zeolites, which have an average pore diameter of 0.51−0.56 nm,[18] anticipating higher catalytic activity to JP-10 (dia: 0.38−0.67 nm).

Upon ignition, emission characteristics from exciting reaction intermediates or products were monitored and identified (Figures 4A and S8), providing insight into the underlying combustion mechanism. The dominant emission characteristic observed in the combustion of all investigated NSMFI(y) doped AlNPs-JP-10 systems is the atomic sodium (Na; $^2S_{1/2} - {}^2P_{1/2}$ and/or $^2S_{1/2} - {}^2P_{3/2}$) line at a wavelength of 589.1 nm.[48] Since, this characteristic is significantly less pronounced in a controlled experiment with a 2 wt % concentration of AlNPs in JP-10 (as impurities only) compared to other NSMFI(y) doped AlNPs-JP-10 zeolite systems, the substantial release of Na during the combustion of NSMFI(y) doped AlNPs-JP-10 droplets may be strongly associated with one of the primary components, Na_2O, present in NSMFI(y) zeolites. It implies that NSMFI(y) zeolites burn extensively after taking part in the catalytic combustion process and releasing Na. The species hydroxyl (OH; $A^2\Sigma^+ \rightarrow X^2\Pi$), methylidyne (CH; $A^2\Delta \rightarrow X^2\Pi$), and water ($H_2O$), which are major intermediates or products of JP-10 combustion, are identified. Recent electronic structure calculations revealed that the decomposition of JP-10 is initiated by the C−H bond cleavages forming six distinct JP-10 carbon-centered ($C_{10}H_{15}$) radicals (Scheme 2B, R1−R6) followed by strained C−C bonds rupture.[54] Moreover, approximately 92% of the decomposition of JP-10 is governed following hydrogen abstraction reaction mechanism.[12] The Brønsted acid sites in NSMFI(y) zeolites are the bridging hydroxyl groups between the Al and Si tetrahedral centers. Taking into account the strong acidity of NSMFI(y) zeolites,[55] the oxygen centers are protonated to mask; hence, JP-10 activation by the hydroxyl groups of zeolites become less feasible. Rather than NSMFI(y) zeolites react with molecular oxygen at raised temperature upon expansion due to the diffusional trapping of high velocity species in droplets forming a hydroxyl (OH) radical by transferring the H atom. The released OH then abstracts one hydrogen atom from the JP-10 molecule in the gas phase resulting the formation of ($C_{10}H_{15}$) radicals, thereby initiating the propagation chain that leads to the desired products including OH with CH and H_2O. The gas phase C−H activation energy of the simplest saturated hydrocarbon methane is 415 kJ mol^{-1}, which is comparable to the C−H activation energy of JP-10 as mention in the scheme. However,

Scheme 2. Formation Pathways for Reactive Species in NSMFI(y) Zeolites Doped with AlNPs-JP-10 Catalytic Combustion (A) and Hydrogen Abstraction Mechanism (B)[a]

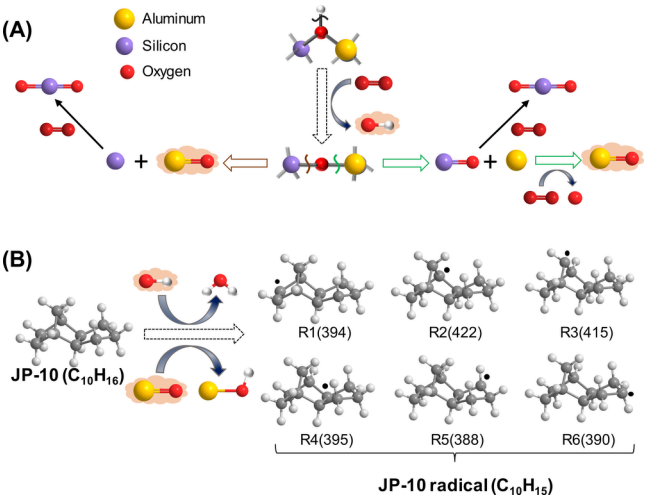

[a]The reaction energies for C−H bond ruptures of unimolecular decomposition of JP-10 are adopted from literature[54] and given in kJ mol^{-1}.

in the presence of OH radicals, methane's energy barrier decreased to 10 kJ mol^{-1}.[56] Low temperature ignition of JP-10 by OH radical was also reported where hydrogen abstractions predominantly occur from secondary carbon sites in JP-10[12]. The substantial decrease in barrier energy in C−H bond activation of hydrocarbons in the presence of OH radicals suggests that this reaction occurred, with the OH radical acting as a key scavenger in the ignition process. Another study has also shown a comparable phenomenon in which the catalyst interacts with the oxidant (H_2O_2) instead of the substrate, cyclohexane hydrocarbon. This interaction leads to the formation of radicals such as hydroxyl (OH), which subsequently removes a hydrogen atom from the substrate cyclohexane followed by the formation of end products.[57] Subsequently, the Al−O−Si generates atomic Al and SiO (silicon monoxide) as a favorable pathway due to the lower bond dissociation energy of AlO (512 kJ mol^{-1}) than SiO (798 kJ mol^{-1}), followed by oxidation of Al to AlO and stable SiO_2, respectively. In contrast, the breakage of the Si−O bond of Al−O−Si directly produces AlO at elevated temperatures during combustion (Scheme 2A).

Additional observations encompass aluminum monoxide (AlO; $A^2\Sigma^+ \rightarrow X^2\Sigma^+$) as one of the key species formed in situ. The formation of AlO might originate from the zeolite Al−O−Si motif, from where the initial OH radical was released via the aforementioned mechanism. It could also be linked to the decomposition/oxidation of AlNPs.[15,58] Our recent investigations have revealed that the gas-phase AlO formation can enhance the catalytic combustion of JP-10 by extracting hydrogen, leading to the generation of AlOH and JP-10 radicals initiated via the formation of van der Waals complexes in the entrance channel by weakly stabilized of 8−48 kJ mol^{-1}, which then undergo a unimolecular decomposition to generate smaller reaction products.[59]

The temporal profiles associated with the species present in the luminous flame resulting from the combustion were retrieved and displayed in Figures 4B and S9. Their time traces

https://doi.org/10.1021/acsami.4c12078
ACS Appl. Mater. Interfaces 2024, 16, 53938−53949

exhibit a rapid increase after ignition commences and reach a maximum, followed by a gradual decrease to the baseline level over the next 15 ± 5 ms. This time period serves to reaffirm the duration of the initial glowing phase. The simultaneous existence of Na with other identified species (OH, CH, AlO, and H_2O) indicates that the ignition was facilitated either by NSMFI(y) zeolites with AlNPs acting as heat transfer carriers, or by both zeolite and AlNPs. Considering the pathways offered by NSMFI(y) zeolites, the zeolite system with the highest Al/Si composition is expected to have the greatest catalytic activity against AlNPs-JP-10. To verify this statement, each system's combustion efficiency was calculated from their corresponding FTIR measurement.

The analysis of the FTIR spectra obtained from the combustion of NSMFI(y) doped AlNPs-JP-10 droplets revealed a significant increase in the signal ratios of CO_2 (at 2170 to 2460 cm^{-1}) to unreacted JP-10 (at 2840 to 3000 cm^{-1}) in comparison to the reference system. It implies that NSMFI(y) zeolites significantly improve the catalytic combustion of AlNPs-JP-10. Although all five zeolites have similar pore sizes of 7.5 ± 0.5 nm, for NSMFI(150)/AlNPs-JP-10 to NSMFI(60)/AlNPs-JP-10, the combustion efficiency rises from 41 to 80%. It could be related to the fact that the number of acidic sites in zeolite systems rises from 0.14 to 0.40 mmol g^{-1}, respectively. These findings are consistent with the aforementioned statement and may help our understanding of the function of acidic sites better in the zeolite-catalyzed combustion mechanism of AlNPs-JP-10. Previous research on the AlNPs-JP-10 system demonstrated that the formation of gas-phase reaction intermediates or products is driven by simple catalytic combustion of JP-10 via hydrogen abstraction by AlO or atomic oxygen (O) as a viable pathway.[60] The initial products AlO or O are formed when the surface of AlNPs, composed of inert Al_2O_3, fractures, exposing the aluminum core to exoergic oxidation with an energy of −15 kJ mol^{-1}. Likewise, hydrogen abstraction from JP-10 by molecular oxygen (O_2) or aluminum (Al) is endothermic and is not considered further. The absence of an O or OH signal in the UV−vis spectrum of the reference system suggest that the JP-10 radical ($C_{10}H_{15}$) is also formed through hydrogen abstraction by AlO. Unlike the reference system, the incorporation of these NSMFI(y) zeolite materials to AlNPs-JP-10 fluid fuel results in multicomponent mixed fuel systems. When it comes to multicomponent systems, the ignition of JP-10 can be triggered by either zeolite or AlNPs, or perhaps both. In addition to the aforementioned pathways for JP-10 activation by OH, the presence of AlO in all zeolite systems confirms zeolites' active participation in the catalytic combustion process, which may be launched by a reaction with oxygen, followed by the abstraction of H atoms from JP-10 to produce $C_{10}H_{15}$ radicals. The presence of acidic sites in NSMFI(y) zeolites might enhance the production of OH and AlO; therefore, NSMFI(60) with a higher concentration of acidic sites is expected to exhibit a reduced ignition delay.

Once the ignition is initiated, it is crucial to maintain continuous and prolonged burning in order to achieve complete combustion. The maximum thickness of the NSMFI(y) zeolite sheets is 2.2 ± 0.5 nm, and they have a pore diameter of 7.5 ± 0.5 nm. These features limit coke formation in the channels and promote diffusion efficiency through knudsen and intercrystalline diffusion of NSMFI(y).[35] It is noted that the macropore (over 50 nm pore diameter) is incomparably larger than the molecular size of high density fuel molecules, including JP-10; nonetheless, the mesopore is more relevant. As a result, the overall burning time is 60 ± 10 ms, compared to 30 ± 10 ms in other droplet combustion systems using nanofluids.[7] Although the burn time is nearly the same, the combustion efficiency changes depending on the acidity concentration of the zeolites, implying a facilitated combustion of JP-10 in the presence of NSMFI(60) zeolite rather than in the presence of NSMFI(150). Additionally, the supply of an abundant pool of reactive oxidant throughout the ignition extends the process with greater efficiency. Evidently, our NSMFI(y) zeolites, having strong acidity and large mesoporosity, as well as a sheet thickness of 2.2 ± 0.5 nm, achieved a combustion efficiency of up to 80 ± 6%.

5. CONCLUSIONS

In conclusion, we investigated the nanosheet MFI zeolite-catalyzed combustion of aluminum nanoparticle-aided exotetrahydrodicyclopentadiene (JP-10) mixed energetic fuel droplets levitated in an oxygen−argon atmosphere by exploiting time-resoled imaging (optical and infrared thermal) and spectroscopic techniques (UV−vis and FTIR). The addition of only 1.0 wt % of NSMFI(y) zeolites to AlNPs-JP-10 fluid fuel lowers the ignition delay, boosts the ignition temperature, and increases the burning time, implying that these NSMFI(y) zeolites are critical in the ignition and sustained combustion of the igniting droplet. The UV−vis emission spectra corroborate the production of the species OH, CH, AlO, H_2O, and Na, providing insight into the chemistry involved in the ignition stages of combustion; whereas, the prolonged emission duration implies ongoing combustion. The formation of the above-mentioned species has been explained by the initiation reaction of zeolite with molecular oxygen upon expansion of the droplets forming hydroxyl (OH) radicals, which then abstracts one hydrogen atom from the JP-10 resulting in the formation of ($C_{10}H_{15}$) radicals thereby initiating the propagation chain that leads to the desired products. Alternatively, these products could have evolved as a result of the decomposition of ($C_{10}H_{15}$) radicals, which are created via hydrogen abstraction of JP-10 by AlO generated during the oxidation of zeolites and/or AlNPs. However, it is obvious that the NSMFI(y) zeolites with strong acidity and substantial mesoporosity are associated with the increased combustion efficiency reaching 80 ± 6% with sustained combustion. Thus, the findings will aid in the development of next-generation sustainable revolutionary multicomponent nanofluid fuels.

■ ASSOCIATED CONTENT

Supporting Information

The Supporting Information is available free of charge at https://pubs.acs.org/doi/10.1021/acsami.4c12078.

Experimental procedure for the preparation of $C_{22-6-6}Br_2$ surfactant; Techniques for characterization of nanosheet MFI zeolite; Experimental methods for Raman analysis; Photo of experimental setup; N_2 adsorption isotherms of five NSMFI(y) zeolites; NH_3-TPD profiles of the NSMFI(y) zeolites; Raman spectra of five NSMFI(y) zeolites; Raman spectra of JP-10, JP-10/AlNPs, JP-10/NSMFI(y), and JP-10/NSMFI(y)/AlNPs; Time-resolved optical imaging of JP-10 droplets doped with NSMFI(y)/AlNPs combustion; 3D plots of UV−vis emission spectra of JP-10 droplets doped with

https://doi.org/10.1021/acsami.4c12078
ACS Appl. Mater. Interfaces 2024, 16, 53938−53949

NSMFI(y)/AlNPs; Deconvoluted UV−vis emission spectra of JP-10 droplets doped with NSMFI(y)/AlNPs; Temporal profiles of the species detected during JP-10 droplets doped with NSMFI(y)/AlNPs combustion; Calibration of FTIR signal for carbon dioxide (CO_2) measurement; Acidity content of NSMFI(y) zeolites; Raman peaks or bands of NSMFI zeolites; Raman peaks or bands of JP-10 and JP-10 containing AlNPs, NSMFI, and NSMFI/AlNPs; Vibrational mode assignments for the peaks and bands of gaseous products during ignition of JP-10 droplets doped with NSMFI(y)/AlNPs (PDF)

AUTHOR INFORMATION

Corresponding Authors

Ralf I. Kaiser − *Department of Chemistry, University of Hawai'i at Manoa, Honolulu, Hawaii 96822, United States;* orcid.org/0000-0002-7233-7206; Email: ralfk@hawaii.edu

Kyungsu Na − *Department of Chemistry, Chonnam National University, Gwangju 61186, South Korea;* orcid.org/0000-0001-5591-449X; Email: kyungsu_na@chonnam.ac.kr

Michelle L. Pantoya − *Mechanical Engineering Department, Texas Tech University, Lubbock, Texas 79409, United States;* orcid.org/0000-0003-0299-1832; Email: michelle.pantoya@ttu.edu

Authors

Dababrata Paul − *Department of Chemistry, University of Hawai'i at Manoa, Honolulu, Hawaii 96822, United States;* orcid.org/0000-0002-5264-3601

Souvick Biswas − *Department of Chemistry, University of Hawai'i at Manoa, Honolulu, Hawaii 96822, United States;* orcid.org/0000-0002-1643-2663

Hyeonji Yeom − *Department of Chemistry, Chonnam National University, Gwangju 61186, South Korea;* orcid.org/0009-0006-9844-0160

Complete contact information is available at: https://pubs.acs.org/10.1021/acsami.4c12078

Notes

The authors declare no competing financial interest.

ACKNOWLEDGMENTS

The Hawaii group was supported by the United States Office of Naval Research (ONR) under Contract N00014-22-1-2010. H.Y. and K.N. are grateful for financial support by the National Research Foundation of Korea (NRF) grant funded by Korea government (MSIT) (RS-2024-00349276). M.P. is grateful for support from United States Office of Naval Research (ONR) Grant Number N00014-22-2006.

REFERENCES

(1) E, X.-T.-F.; Zhang, L.; Wang, F.; Zhang, X.; Zou, J.-J. Synthesis of Aluminum Nanoparticles as Additive to Enhance Ignition and Combustion of High Energy Density Fuels. *Front. Chem. Sci. Eng.* **2018**, *12*, 358−366.

(2) Chen, B. H.; Liu, J. Z.; Li, H. P.; Yang, W. J.; Cen, K. F. Laser Ignition and Combustion Characteristics of Al/JP-10 Nanofluid Droplet. *J. Therm. Anal. Calorim.* **2019**, *135*, 925−934.

(3) Lucas, M.; Brotton, S. J.; Min, A.; Pantoya, M. L.; Kaiser, R. I. Oxidation of Levitated exo-Tetrahydrodicyclopentadiene Droplets Doped with Aluminum Nanoparticles. *J. Phys. Chem. Lett.* **2019**, *10*, 5756−5763.

(4) Stanmore, B.; Brilhac, J.-F.; Gilot, P. The Ignition and Combustion of Cerium Doped Diesel Soot. *SAE Trans.* **1999**, *108*, 75−81.

(5) Allen, C.; Mittal, G.; Sung, C.-J.; Toulson, E.; Lee, T. An Aerosol Rapid Compression Machine for Studying Energetic-Nanoparticle-Enhanced Combustion of Liquid Fuels. *Proc. Combust. Inst.* **2011**, *33*, 3367−3374.

(6) Jin, Y.; Dou, S.; Yang, Q.; Xu, X.; Fu, Q.; Pan, L. Performance Characteristics of a Scramjet Engine Using JP-10 Fuel Containing Aluminum Nanoparticles. *Acta Astronaut.* **2021**, *185*, 70−77.

(7) Antonov, I.; Chyba, A.; Perera, S. D.; Turner, A. M.; Pantoya, M. L.; Finn, M. T.; Epshteyn, A.; Kaiser, R. I. Discovery of Discrete Stages in the Oxidation of exo-Tetrahydrodicyclopentadiene ($C_{10}H_{16}$) Droplets Doped with Titanium−Aluminum−Boron Reactive Mixed-Metal Nanopowder. *J. Phys. Chem. Lett.* **2022**, *13*, 9777−9785.

(8) Jin, Y.; Xu, X.; Wang, X.; Dou, S.; Yang, Q.; Pan, L. Propulsive and Combustion Behavior of Hydrocarbon Fuels Containing Boron Nanoparticles in a Liquid Rocket Combustor. *Proc. Inst. Mech. Eng. G: J. Aerosp. Eng.* **2022**, *236*, 2580−2591.

(9) Chung, H. S.; Chen, C. S. H.; Kremer, R. A.; Boulton, J. R.; Burdette, G. W. Recent Developments in High-Energy Density Liquid Hydrocarbon Fuels. *Energy Fuels* **1999**, *13*, 641−649.

(10) Colket, M. B.; Spadaccini, L. J. Scramjet Fuels Autoignition Study. *J. Propul. Power* **2001**, *17*, 315−323.

(11) Edwards, T. Liquid Fuels and Propellants for Aerospace Propulsion: 1903−2003. *J. Propul. Power* **2003**, *19*, 1089−1107.

(12) Gao, C. W.; Vandeputte, A. G.; Yee, N. W.; Green, W. H.; Bonomi, R. E.; Magoon, G. R.; Wong, H.-W.; Oluwole, O. O.; Lewis, D. K.; Vandewiele, N. M.; Van Geem, K. M. JP-10 Combustion Studied with Shock Tube Experiments and Modeled with Automatic Reaction Mechanism Generation. *Combust. Flame* **2015**, *162*, 3115−3129.

(13) Li, G.; Hou, B.; Wang, A.; Xin, X.; Cong, Y.; Wang, X.; Li, N.; Zhang, T. Making JP-10 Superfuel Affordable with a Lignocellulosic Platform Compound. *Angew. Chem., Int. Ed. Engl.* **2019**, *58*, 12154−12158.

(14) Bruno, T. J.; Huber, M. L.; Laesecke, A.; Lemmon, E. W.; Perkins, R. A. Thermochemical and Thermophysical Properties of JP-10. *Technical Report NISTIR* **2006**, *6640*, 325.

(15) Biswas, S.; Paul, D.; Dias, N.; Lu, W.; Ahmed, M.; Pantoya, M. L.; Kaiser, R. I. Efficient Oxidative Decomposition of Jet-Fuel exo-Tetrahydrodicyclopentadiene (JP-10) by Aluminum Nanoparticles in a Catalytic Microreactor: An Online Vacuum Ultraviolet Photoionization Study. *J. Phys. Chem. A* **2024**, *128*, 1665−1684.

(16) Liu, J. Z.; Chen, B. H.; Wu, T. T.; Yang, W. J.; Zhou, J. H. Ignition and Combustion Characteristics and Agglomerate Evolution Mechanism of Aluminum in nAl/JP-10 Nanofluid fuel. *J. Therm. Anal. Calorim.* **2019**, *137*, 1369−1379.

(17) Biswas, S.; Paul, D.; Dias, N.; Kunzler, K.; Ahmed, M.; Pantoya, M. L.; Kaiser, R. I. Stress-Alteration Enhancement of the Reactivity of Aluminum Nanoparticles in the Catalytic Decomposition of exo-Tetrahydrodicyclopentadiene (JP-10). *J. Phys. Chem. A* **2024**, *128*, 3613−3624.

(18) Perera, S. D.; Brotton, S. J.; Shinsato, H.; Kaiser, R. I.; Choi, Y.; Na, K. Catalytic Effects of Zeolite Socony Mobil-5 (ZSM-5) on the Oxidation of Acoustically Levitated exo-Tetrahydrodicyclopentadiene (JP-10) Droplets. *J. Phys. Chem. A* **2021**, *125*, 4896−4909.

(19) Yang, Q.; Li, S.; Ye, L.; Huang, X. Understanding of Contradiction on Concentration Effect on Stability, Physical Properties, Evaporation and Microexplosion Characteristics of Al/JP-10/Oleic Acid Nanofluid Fuel. *Nanomaterials (Basel, Switzerland)* **2022**, *12*, 3446.

(20) Truitt, M. J.; Toporek, S. S.; Rovira-Truitt, R.; White, J. L. Alkane C−H Bond Activation in Zeolites: Evidence for Direct Protium Exchange. *J. Am. Chem. Soc.* **2006**, *128*, 1847−1852.

(21) Wu, Y.; Emdadi, L.; Oh, S. C.; Sakbodin, M.; Liu, D. Spatial Distribution and Catalytic Performance of Metal−Acid Sites in Mo/

MFI Catalysts with Tunable Meso-/Microporous Lamellar Zeolite Structures. *J. Catal.* **2015**, *323*, 100−111.
(22) Jaegers, N. R.; Khivantsev, K.; Kovarik, L.; Klas, D. W.; Hu, J. Z.; Wang, Y.; Szanyi, J. Catalytic Activation of Ethylene C−H Bonds on Uniform d^8 Ir(i) and Ni(ii) Cations in Zeolites: Toward Molecular Level Understanding of Ethylene Polymerization on Heterogeneous Catalysts. *Catal. Sci. Technol.* **2019**, *9*, 6570−6576.
(23) Liu, B.; Chen, Z.; Huang, J.; Chen, H.; Fang, Y. Direct Synthesis of Hierarchically Structured MFI Zeolite Nanosheet Assemblies with Tailored Activity in Benzylation Reaction. *Microporous Mesoporous Mater.* **2019**, *273*, 235−242.
(24) Bickel, E. E.; Gounder, R. Hydrocarbon Products Occluded within Zeolite Micropores Impose Transport Barriers that Regulate Brønsted Acid-Catalyzed Propene Oligomerization. *JACS Au* **2022**, *2*, 2585−2595.
(25) Chen, L.; Deng, Y.; Han, W.; E, J.; Wang, C.; Han, D.; Feng, C. Effects of Zeolite Molecular Sieve on the Hydrocarbon Adsorbent and Diffusion Performance of Gasoline Engine During Cold Start. *Fuel* **2022**, *310*, 122427.
(26) Xue, W.; Mei, D. Mechanistic Understanding of Methane Combustion Over H-SSZ-13 Zeolite Encapsulated Palladium Nanocluster Catalysts. *Chem. Eng. J.* **2022**, *444*, 136671.
(27) Zhou, Y.; Santos, S.; Shamzhy, M.; Marinova, M.; Blanchenet, A.-M.; Kolyagin, Y. G.; Simon, P.; Trentesaux, M.; Sharna, S.; Ersen, O.; Zholobenko, V. L.; Saeys, M.; Khodakov, A. Y.; Ordomsky, V. V. Liquid Metals for Boosting Stability of Zeolite Catalysts in the Conversion of Methanol to Hydrocarbons. *Nat. Commun.* **2024**, *15*, 2228.
(28) Kim, J.; Hyeon, D. H.; Park, S. H.; Chun, B.-H.; Jeong, B. H.; Han, J. S.; Kim, S. H. Catalytic Endothermic Reactions of exo-Tetrahydrodicyclopentadiene with Zeolites and Improvement of Heat of Reactions. *Catal. Today* **2014**, *232*, 63−68.
(29) Choi, M.; Na, K.; Kim, J.; Sakamoto, Y.; Terasaki, O.; Ryoo, R. Stable Single-Unit-Cell Nanosheets of Zeolite MFI as Active and Long-Lived Catalysts. *Nature* **2009**, *461*, 246−249.
(30) Kim, K.; Ryoo, R.; Jang, H.-D.; Choi, M. Spatial Distribution, Strength, and Dealumination Behavior of Acid Sites in Nanocrystalline MFI Zeolites and Their Catalytic Consequences. *J. Catal.* **2012**, *288*, 115−123.
(31) Shamzhy, M.; Gil, B.; Opanasenko, M.; Roth, W. J.; Čejka, J. MWW and MFI Frameworks as Model Layered Zeolites: Structures, Transformations, Properties, and Activity. *ACS Catal.* **2021**, *11*, 2366−2396.
(32) Meng, X.; Nawaz, F.; Xiao, F.-S. Templating Route for Synthesizing Mesoporous Zeolites with Improved Catalytic Properties. *Nano Today* **2009**, *4*, 292−301.
(33) Na, K.; Choi, M.; Ryoo, R. Recent Advances in the Synthesis of Hierarchically Nanoporous Zeolites. *Microporous Mesoporous Mater.* **2013**, *166*, 3−19.
(34) Xiao, X.; Zhang, Y.; Jiang, G.; Liu, J.; Han, S.; Zhao, Z.; Wang, R.; Li, C.; Xu, C.; Duan, A.; Wang, Y.; Liu, J.; Wei, Y. Simultaneous Realization of High Catalytic Activity and Stability for Catalytic Cracking of n-Heptane on Highly Exposed (010) Crystal Planes of Nanosheet ZSM-5 Zeolite. *Chem. Commun.* **2016**, *52*, 10068−10071.
(35) Tian, Y.; Qiu, Y.; Hou, X.; Wang, L.; Liu, G. Catalytic Cracking of JP-10 over HZSM-5 Nanosheets. *Energy Fuel* **2017**, *31*, 11987−11994.
(36) Lim, S.; Song, Y.; Jeong, K.; Park, J. H.; Na, K. Enhanced Dehydrogenative H_2 Release from N-Containing Amphicyclic LOHC Boosted by Pd-Supported Nanosheet MFI Zeolites Having Strong Acidity and Large Mesoporosity. *ACS Sustain. Chem. Eng.* **2022**, *10*, 3584−3594.
(37) Gesner, J.; Pantoya, M. L.; Levitas, V. I. Effect of Oxide Shell Growth on Nano-Aluminum Thermite Propagation Rates. *Combust. Flame* **2012**, *159*, 3448−3453.
(38) Na, K.; Park, W.; Seo, Y.; Ryoo, R. Disordered Assembly of MFI Zeolite Nanosheets with a Large Volume of Intersheet Mesopores. *Chem. Mater.* **2011**, *23*, 1273−1279.
(39) Brotton, S. J.; Kaiser, R. I. Novel High-Temperature and Pressure-Compatible Ultrasonic Levitator Apparatus Coupled to Raman and Fourier Transform Infrared Spectrometers. *Rev. Sci. Instrum.* **2013**, *84*, na.
(40) Brotton, S. J.; Lucas, M.; Chambreau, S. D.; Vaghjiani, G. L.; Yu, J.; Anderson, S. L.; Kaiser, R. I. Spectroscopic Investigation of the Primary Reaction Intermediates in the Oxidation of Levitated Droplets of Energetic Ionic Liquids. *J. Phys. Chem. Lett.* **2017**, *8*, 6053−6059.
(41) Biswas, S.; Antonov, I.; Fujioka, K.; Rizzo, G. L.; Chambreau, S. D.; Schneider, S.; Sun, R.; Kaiser, R. I. Unraveling the Initial Steps of the Ignition Chemistry of the Hypergolic Ionic Liquid 1-Ethyl-3-Methylimidazolium Cyanoborohydride ([EMIM][CBH]) with nitric acid (HNO_3) Exploiting Chirped Pulse Triggered Droplet Merging. *Phys. Chem. Chem. Phys.* **2023**, *25*, 6602−6625.
(42) Rizzo, G. L.; Biswas, S.; Antonov, I.; Miller, K. K.; Pantoya, M. L.; Kaiser, R. I. Exotic Inverse Kinetic Isotopic Effect in the Thermal Decomposition of Levitated Aluminum Iodate Hexahydrate Particles. *J. Phys. Chem. Lett.* **2023**, *14*, 2722−2730.
(43) Biswas, S.; Fujioka, K.; Antonov, I.; Rizzo, G. L.; Chambreau, S. D.; Schneider, S.; Sun, R.; Kaiser, R. I. Hypergolic Ionic Liquids: to be or Not to be? *Chem. Sci.* **2024**, *15*, 1480−1487.
(44) Rizzo, G.; Biswas, S.; Pantoya, M.; Kaiser, R. Unraveling the Ignition Chemistry of Singly Levitated Aluminum Iodate Hexahydrate (AIH) Particles. *Chem. Phys. Lett.* **2024**, *842*, 141212.
(45) Mortier, W. J.; Bosmans, H. J. Location of Univalent Cations in Synthetic Zeolites of the Y and X Type with Varying Silicon to Aluminum Ratio. I. Hydrated Potassium Exchanged Forms. *J. Phys. Chem.* **1971**, *75* (21), 3327.
(46) Hernandez-Tamargo, C. E.; Roldan, A.; de Leeuw, N. H. A Density Functional Theory Study of the Structure of Pure-Silica and Aluminium-Substituted MFI Nanosheets. *J. Solid State Chem.* **2016**, *237*, 192.
(47) Attila, Ö.; King, H. E.; Meirer, F.; Weckhuysen, B. M. 3D Raman Spectroscopy of Large Zeolite ZSM-5 Crystals. *Chem.—Eur. J.* **2019**, *25*, 7158−7167.
(48) McCrary, P. D.; Beasley, P. A.; Cojocaru, O. A.; Schneider, S.; Hawkins, T. W.; Perez, J. P. L.; McMahon, B. W.; Pfeil, M.; Boatz, J. A.; Anderson, S. L.; Son, S. F.; Rogers, R. D. Hypergolic Ionic Liquids to Mill, Suspend, and Ignite Boron Nanoparticles. *Chem. Commun.* **2012**, *48*, 4311−4313.
(49) Brotton, S. J.; Kaiser, R. I. In Situ Raman Spectroscopic Study of Gypsum ($CaSO_4{\cdot}2H_2O$) and Epsomite ($MgSO_4{\cdot}7H_2O$) Dehydration Utilizing an Ultrasonic Levitator. *J. Phys. Chem. Lett.* **2013**, *4*, 669−673.
(50) Brotton, S. J.; Lucas, M.; Jensen, T. N.; Anderson, S. L.; Kaiser, R. I. Spectroscopic Study on the Intermediates and Reaction Rates in the Oxidation of Levitated Droplets of Energetic Ionic Liquids by Nitrogen Dioxide. *J. Phys. Chem. A* **2018**, *122*, 7351−7377.
(51) Linstrom, P. J.; Mallard, W. G. The NIST Chemistry WebBook: A Chemical Data Resource on the Internet. *J. Chem. Eng. Data* **2001**, *46*, 1059−1063.
(52) Gordon, I. E.; Rothman, L. S.; Hill, C.; Kochanov, R. V.; Tan, Y.; Bernath, P. F.; Birk, M.; Boudon, V.; Campargue, A.; Chance, K. V.; Drouin, B. J.; Flaud, J. M.; Gamache, R. R.; Hodges, J. T.; Jacquemart, D.; Perevalov, V. I.; Perrin, A.; Shine, K. P.; Smith, M. A. H.; Tennyson, J.; Toon, G. C.; Tran, H.; Tyuterev, V. G.; Barbe, A.; Császár, A. G.; Devi, V. M.; Furtenbacher, T.; Harrison, J. J.; Hartmann, J. M.; Jolly, A.; Johnson, T. J.; Karman, T.; Kleiner, I.; Kyuberis, A. A.; Loos, J.; Lyulin, O. M.; Massie, S. T.; Mikhailenko, S. N.; Moazzen-Ahmadi, N.; Müller, H. S. P.; Naumenko, O. V.; Nikitin, A. V.; Polyansky, O. L.; Rey, M.; Rotger, M.; Sharpe, S. W.; Sung, K.; Starikova, E.; Tashkun, S. A.; Auwera, J. V.; Wagner, G.; Wilzewski, J.; Wcisło, P.; Yu, S.; Zak, E. J. The HITRAN2016 Molecular Spectroscopic Database. *J. Quant. Spectrosc. Radiat. Transfer* **2017**, *203*, 3−69.
(53) Brotton, S. J.; Malek, M. J.; Anderson, S. L.; Kaiser, R. I. Effects of Acetonitrile-Assisted Ball-Milled Aluminum Nanoparticles on the

https://doi.org/10.1021/acsami.4c12078
ACS Appl. Mater. Interfaces 2024, 16, 53938−53949

Ignition of Acoustically Levitated Exo-Tetrahydrodicyclopentadiene (JP-10) Droplets. *Chem. Phys. Lett.* **2020**, *754*, 137679.
(54) Zhao, L.; Yang, T.; Kaiser, R. I.; Troy, T. P.; Xu, B.; Ahmed, M.; Alarcon, J.; Belisario-Lara, D.; Mebel, A. M.; Zhang, Y.; Cao, C.; Zou, J. A Vacuum Ultraviolet Photoionization Study on High-Temperature Decomposition of JP-10 (exo-Tetrahydrodicyclopentadiene). *Phys. Chem. Chem. Phys.* **2017**, *19*, 15780−15807.
(55) Seo, Y.; Cho, K.; Jung, Y.; Ryoo, R. Characterization of the Surface Acidity of MFI Zeolite Nanosheets by ^{31}P NMR of Adsorbed Phosphine Oxides and Catalytic Cracking of Decalin. *ACS Catal.* **2013**, *3*, 713−720.
(56) Larsson, A.; Zettervall, N.; Hurtig, T.; Nilsson, E. J. K.; Ehn, A.; Petersson, P.; Alden, M.; Larfeldt, J.; Fureby, C. Skeletal Methane−Air Reaction Mechanism for Large Eddy Simulation of Turbulent Microwave-Assisted Combustion. *Energy Fuel* **2017**, *31*, 1904−1926.
(57) Ribeiro, A. P. C.; Martins, L. M. D. R. S.; Hazra, S.; Pombeiro, A. J. L. Catalytic Oxidation of Cyclohexane with Hydrogen Peroxide and a Tetracopper(II) Complex in an Ionic Liquid. *C. R. Chim.* **2015**, *18*, 758−765.
(58) Biswas, S.; Paul, D.; He, C.; Dias, N.; Ahmed, M.; Pantoya, M. L.; Kaiser, R. I. Counterintuitive Catalytic Reactivity of the Aluminum Oxide "Passivation" Shell of Aluminum Nanoparticles Facilitating the Thermal Decomposition of exo-Tetrahydrodicyclopentadiene (JP-10). *J. Phys. Chem. Lett.* **2023**, *14*, 9341−9350.
(59) Brotton, S. J.; Perera, S. D.; Misra, A.; Kleimeier, N. F.; Turner, A. M.; Kaiser, R. I.; Palenik, M.; Finn, M. T.; Epshteyn, A.; Sun, B. J.; Zhang, L. J.; Chang, A. H. H. Combined Spectroscopic and Computational Investigation on the Oxidation of exo-Tetrahydrodicyclopentadiene (JP-10; $C_{10}H_{16}$) Doped with Titanium-Aluminum-Boron Reactive Metal Nanopowder. *J. Phys. Chem. A* **2022**, *126*, 125−144.
(60) Lucas, M.; Brotton, S. J.; Min, A.; Woodruff, C.; Pantoya, M. L.; Kaiser, R. I. Effects of Size and Prestressing of Aluminum Particles on the Oxidation of Levitated exo-Tetrahydrodicyclopentadiene Droplets. *J. Phys. Chem. A* **2020**, *124*, 1489−1507.

https://doi.org/10.1021/acsami.4c12078
ACS Appl. Mater. Interfaces 2024, 16, 53938−53949